INTERNATIONAL JOURNAL FOR NUMERICAL METHODS IN FLUIDS
Int. J. Numer. Meth. Fluids 2005; **49**:635–655
Published online 24 June 2005 in Wiley InterScience (www.interscience.wiley.com). DOI: 10.1002/fld.1022

Investigation of two-dimensional channel flow with a partially compliant wall using finite volume–finite difference approach

X. Zhang[1,2,*,†], R. Ajaykumar[1], N. M. Sudharsan[1,3] and K. Kumar[1]

[1]*CFD Division, Institute of High Performance Computing, Singapore Science Park II, Singapore 117528, Singapore*
[2]*LNM, Institute of Mechanics, Chinese Academy of Sciences, Beijing 100080, People's Republic of China*
[3]*Department of Mechanical Engineering, College of Engineering, Anna University, Guindy, 600 025, India*

SUMMARY

This paper presents a numerical simulation of steady two-dimensional channel flow with a partially compliant wall. Navier–Stokes equation is solved using an unstructured finite volume method (FVM). The deformation of the compliant wall is determined by solving a membrane equation using finite difference method (FDM). The membrane equation and Navier–Stokes equation are coupled iteratively to determine the shape of the membrane and the flow field. A spring analogy smoothing technique is applied to the deformed mesh to ensure good mesh quality throughout the computing procedure. Numerical results obtained in the present simulation match well with that in the literature. Copyright © 2005 John Wiley & Sons, Ltd.

KEY WORDS: compliant wall; Navier–Stokes; finite volume method; finite difference method

1. INTRODUCTION

The flow in a compliant channel is related to many physiological applications. For example, blood flow in arteries and veins, urine flow in the urethras and air flow in the lungs. The compliance of the wall has a great influence on the transport of fluid, and thus will elicit

*Correspondence to: X. Zhang, LNM, Institute of Mechanics, Chinese Academy of Sciences, Beijing 100080, People's Republic of China.
†E-mail: zhangx@lnm.imech.ac.cn

Contract/grant sponsor: Institute of High Performance Computing (IHPC); contract/grant number: IHPC/02-100325-EOM

Received 6 October 2003
Revised 18 October 2004
Accepted 17 May 2005

Copyright © 2005 John Wiley & Sons, Ltd.

important biological effects on the living body. Human snoring and wheezing are two of the phenomena related to the oscillation of walls in human airways.

Motivated by the fundamentals of physiology, this area has attracted many researchers during the past 30 years. Experimental studies date back to the 1960s and 1970s (e.g. References [1, 2]). Large amount of literature references were found from the 1980s and 1990s [3–10]. In the standard experiment, a segment of rubber is mounted at its ends on a rigid tube. These two tubes are placed in a chamber where the pressure could be independently controlled. The behaviour of the system is studied by adjusting the controlling parameters such as the ambient pressure both in the chamber and at the outlet, the material property of the compliant tube such as the tension and the flow rate. A steady flow was obtained in certain range of the controlling parameters. Beyond this range, however, complicated phenomena such as flow-induced oscillations occurs.

The early theoretical studies were based on *ad hoc* one-dimensional models, e.g. References [11–14]. These works did explain some phenomena observed in experiments. In order to perform more realistic simulations, Pedley [15] first studied a steady two-dimensional flow with collapsible wall at low Reynolds number using Stokes approximation for the fluid. Later, two-dimensional simulation by solving full Navier–Stokes equations was done by Luo and Pedley [16, 17] for steady and unsteady flows. The wall was modelled as an elastic membrane of zero thickness. In this model, the wall only moves vertically, the longitudinal stretch and bending stiffness of the material are neglected. Heil [18, 19] performed a three-dimensional simulation of flow through a collapsible tube using Stokes approximation for the fluid and a shell model for the wall. Recently, a more realistic model was proposed by Cai and Luo [20], in which a plane strained elastic beam with large deflection and incrementally linear extension was used to replace the membrane. Bathe and Kamm [21], Shim and Kamm [22] solved the two-dimensional Navier–Stokes equation for the fluid and two-dimensional equilibrium equation for the solid elastic wall. In these simulations mentioned above, the effect of certain control parameters on the fluid–solid system was studied by carrying out 'numerical experiments'.

In almost all these numerical studies, finite element method (FEM) was chosen as their numerical scheme, Reference [23] was the only exception in which finite difference method (FDM) was used. Our paper presents an alternative approach to tackle this problem: finite volume method (FVM) is used to solve the fluid equation and finite difference method (FDM) is used to solve the membrane equation. Although FVM is the most popular numerical method in the area of computational fluid dynamics (CFD), in research areas where the fluid and structure interaction (FSI) is involved, FEM still dominates. This is because FEM is traditionally the only choice for structural analysis. It is only recently that FVM has begun to play a role in this area. Demirdzic and Martinovic [24] and Demirdzic and Muzaferijia [25] presented a stress analysis using FVM. Slone *et al.* [26] even presented a solution strategy of using FVM for both the fluid and the structure. The advantage of FVM lies in its simplicity of formulation and attractive local conservation properties.

This paper presents an investigation of the compliant channel flow problem using FVM–FDM approach. Section 1 gives the governing equation and numerical schemes for the fluid. Section 2 focuses on solution of the membrane equation. Section 3 explains how the solution to the fluid and membrane are coupled. Section 4 gives the numerical results and discussions. Conclusions and future work plan are given in Section 5.

Copyright © 2005 John Wiley & Sons, Ltd.

2. SOLUTION TO THE FLUID DOMAIN

2.1. Governing equations

The motion of the fluid is governed by the following conservation laws written in an integral incompressible form.

The continuity equation:

$$\int_{\partial S} (\mathbf{v} - \mathbf{v}_m) \cdot \mathbf{n} \, dS = 0 \tag{1}$$

The momentum equation:

$$\frac{\partial}{\partial t} \int_V \mathbf{v} \, dV + \int_{\partial S} \left[\mathbf{v}(\mathbf{v} - \mathbf{v}_m) \cdot \mathbf{n} - \frac{1}{Re} (\nabla \mathbf{v}) \cdot \mathbf{n} \right] dS = - \int_{\partial S} P\mathbf{n} \, dS \tag{2}$$

where V is an arbitrary volume occupied by the fluid, P is the pressure. dS is the bounding surface. $\mathbf{v}$ is the velocity of the fluid, $\mathbf{v}_m$ is the velocity of the mesh. $\mathbf{n}$ is the unit normal vector on surface dS. Here Equations (1) and (2) are in a non-dimensional form. Re is the Reynolds number which is defined as

$$Re = \frac{\rho^* u^* L^*}{\mu^*} \tag{3}$$

where ρ^* is the density of the fluid and μ^* is the dynamic viscosity. u^* and L^* are the characteristic velocity and length, respectively. The details of the dimensionless formulation and the choices of the characteristic variables are given in the Appendix.

2.2. Numerical scheme

An unstructured FVM is used to discretize the fluid equations. The method described in References [27, 28] is followed with some modifications. The discretization procedure will only be summarized briefly, for the details, please refer to these papers.

In order to obtain a discrete solution of Equations (1) and (2), the solution domain is discretized into a finite number of contiguous control volumes (CVs) or cells. Only CVs of triangular shape are used in this paper. All dependent variables are stored at the cell centres, i.e. a collocated arrangement is adopted.

The discretization procedure for the momentum equation (2) is explained in the form of a transport equation of an arbitrary variable ϕ:

$$\underbrace{\frac{\partial}{\partial t} \int_V \phi \, dV}_{\text{Rate of change}} + \underbrace{\int_S [\phi(\mathbf{v} - \mathbf{v}_m) - \Gamma_\phi \nabla \phi] \cdot \mathbf{n} \, dS}_{\text{Convection}\quad\text{Diffusion}} = \underbrace{\int_S Q_\phi \, dS}_{\text{Source}} \tag{4}$$

Here ϕ represents the velocity components v_i $(i = 1, 2)$; Γ_ϕ is the diffusive coefficient $(1/Re)$ and the source term is $Q_\phi = -P\mathbf{n}_i$. Body force is not included in all the solution procedures below.

Copyright © 2005 John Wiley & Sons, Ltd.

The rate of change is discretized by a backward Euler (fully implicit) scheme:

$$\frac{\partial}{\partial t}\int_V \phi \, \mathrm{d}V \approx \frac{1}{\Delta t}[(\phi V)^n - (\phi V)^{n-1}] \tag{5}$$

where 'n' and '$n-1$' are the time step counters.

The convective term is discretized as

$$\int_S \phi(\mathbf{v} - \mathbf{v}_\mathrm{m}) \cdot \mathbf{n} \, \mathrm{d}s \approx \dot{m}_j \tilde{\phi}_j \tag{6}$$

where m_j is the volume flux across face j. It is defined as

$$\dot{m}_j = \int_{S_j} (\mathbf{v} - \mathbf{v}_\mathrm{m}) \cdot \mathbf{n} \, \mathrm{d}S \approx A_j(\tilde{\mathbf{v}}_j - \mathbf{v}_\mathrm{m}) \cdot \mathbf{n}_j \tag{7}$$

where A_j is the area of face j; $\tilde{\mathbf{v}}_j$ is the face velocity. The mesh velocities $\mathbf{v}_\mathrm{m}$ are chosen in such a way that they satisfy the space conservation law (SCL). They could be computed by coupling with membrane displacement and mesh smoothing computations. However, if only steady solution is sought, they could also be set to zero for simplicity, although the inclusion of them may improve convergence.

$\tilde{\phi}_j$ is the variable interpolated to face j using a blending scheme

$$\tilde{\phi}_j = \phi_j^{(1)} + \gamma_\phi(\phi_j^{(2)} - \phi_j^{(1)}) \tag{8}$$

Here the superscript '(1)' and '(2)' denote first- and second-order interpolation, respectively. The first-order interpolation is just a simple 'upwind' scheme. The second-order scheme uses the gradient of variable ϕ and Taylor expansion to evaluate the value of ϕ on the face centres. In this paper, the gradient of ϕ is constructed using a least-squares approach. γ_ϕ is a blending factor which is set to 0.95 in this paper.

The diffusion term is discretized as

$$\int_{S_j} -\Gamma_\phi \nabla\phi \cdot \mathbf{n} \, \mathrm{d}S \approx -\Gamma_{\phi j}\frac{A_j}{L_j}((\phi_{P_j} - \phi_{P_0}) + [(\nabla\phi)_{P_j} \cdot \boldsymbol{\tau}_1 - (\nabla\phi)_{P_0} \cdot \boldsymbol{\tau}_2]) \tag{9}$$

Here L_j is the distance from the centre of cell P_0 to that of cell P_j projected to the normal direction on face j. $\boldsymbol{\tau}_1$ and $\boldsymbol{\tau}_2$ are two vectors on the tangential direction of face j (see Figure 1). The first term on the RHS of (9) is the 'normal diffusion' and the second term is the 'cross diffusion' which is a correction for non-orthogonal meshes.

Linear systems are obtained as a result of the discretization of the two velocity components:

$$a_{P_0}^C \phi_{P_0} = \sum_{j=1}^{3} a_{P_0}^j \phi_{P_0}^j + b_{P_0} \tag{10}$$

Here superscript 'C' denotes the diagonal element of the coefficient matrix and 'j' denotes the neighbouring cells which share a common face with cell P_0. The contributions to the coefficient matrix are: the mass matrix, upwind difference of the convective term, the 'normal diffusion'. The source term b_{P_0} in (10) has three contributions, the pressure gradient, the 'cross diffusion', and the departures of the convective flux from the upwind differencing (deferred correction).

Copyright © 2005 John Wiley & Sons, Ltd.

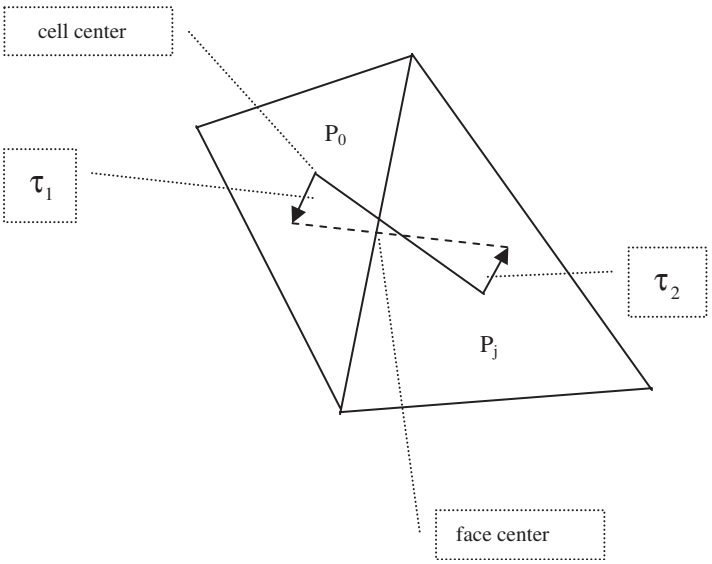

Figure 1. Cells used in the discretization. The dashed line is perpendicular to the cell face. It makes an angle (not necessarily 90°) with the line connecting cell P_0 and P_1.

The *SIMPLE* algorithm is used to calculate the pressure. A pressure-correction equation is derived from the continuity equation (1)

$$\sum_{j=1}^{3} \overline{\left(\frac{1}{a_{P_0}^C}\right)}_j (\nabla p')_j A_j \mathbf{n}_j = \sum_{j=1}^{3} \dot{m}_j \tag{11}$$

where p' is the pressure correction and (—) stands for arithmetic averaging from cell to face.

The LHS of (11) is a Laplacian operator and is treated similarly as the diffusive term in the momentum equation. Some corrections for the mesh non-orthogonality are also considered. After obtaining the pressure correction p', pressure and velocity are corrected by

$$\begin{aligned} p^m &= p^{m-1} + \beta_p p'^m \\ \mathbf{v}^m &= \mathbf{v}^{m-1} - \frac{1}{a_{v_0}} \sum_{j=1}^{3} p_j'^m A_j \mathbf{n}_j \end{aligned} \tag{12}$$

Here β_P is a relaxation factor for pressure, Ferziger and Peric [29] suggested that $\beta_p = 0.2$ for fluid; m is the pressure-correction loop counter at time step n. After the corrections, the coefficient matrix and source term in (10) are computed using the newly updated p and $\mathbf{v}$. A new velocity is obtained by solving (10) again. This velocity is then substituted into (11) to compute a new pressure correction. This pressure-correction procedure is repeated until the convergence criterion is satisfied. Solutions to subsequent time steps are obtained following the same procedure. A steady solution of the flow field is achieved by time marching until the transient term is negligibly small.

Copyright © 2005 John Wiley & Sons, Ltd.

Attentions are to be paid to the face velocity $\tilde{\mathbf{v}}_j$ which is used to calculate the volume flux. This velocity cannot be obtained by a simple average of the values in the neighbouring cells. Instead, a *Rhie-Chow* interpolation which introduces some dependency on the pressure is used. More details can be obtained from Reference [27].

2.3. Boundary and initial conditions

A schematic sketch of the problem under consideration is shown in Figure 2. Four different types of boundary condition are prescribed on these boundaries. They are:

(1) *Inlet*: The velocity is prescribed as the solution of a two-dimensional Poiseuille flow, i.e.

$$\begin{aligned} v_1 &= 6y(1-y) \\ v_2 &= 0 \end{aligned} \tag{13}$$

The normal gradient of pressure is set to zero.

(2) *Outlet*: The pressure is set to a constant (zero). In order to satisfy the continuity constraint, the velocity is corrected using the gradient of pressure correction in a manner similar to (12). This issue has also been addressed in Reference [29].

(3) *Solid and compliant wall*: On the solid walls, all velocity components are zero. For the compliant wall, velocity equals to the velocity of the moving membrane, however, if only steady solution is sought, it could just be set to zero for simplicity. On both the solid wall and the compliant wall, normal gradient of pressure is set to zero.

The initial velocity is the same as (13) and the pressure is a linear function of x, i.e.

$$P = \frac{12}{Re}(L_1 + L_c + L_2 - x) \tag{14}$$

L_1, L_c and L_2 are dimensions of this problem that are shown in Figure 2.

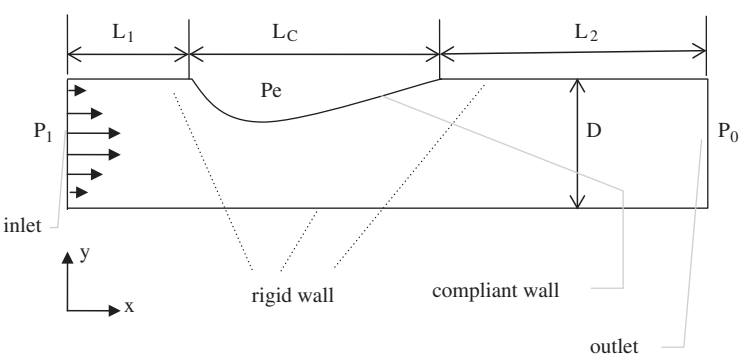

Figure 2. Geometry configuration and boundary types.

Copyright © 2005 John Wiley & Sons, Ltd.

3. SOLUTION TO THE MOTION OF THE COMPLIANT WALL

The compliant wall is modelled as a thin membrane. The governing equation is written in a non-dimensional form as

$$-\frac{Tf''}{(1+f'^2)^{3/2}}+(P-P_e)=0 \tag{15}$$

where f is the membrane displacement (in y-direction), P and P_e are the fluid and ambient pressure acting on the membrane. T is the tension of the membrane.

In this model, the inertia of the membrane is neglected. It is also assumed that the longitudinal variation of tension is negligible, so that T could be treated as a constant. The explanations for these assumptions are given in References [17, 30].

The ODE in (15) is discretized using FDM. Central difference is used to discretized the second derivative. The final form is written as

$$\frac{\Delta_{i+1}}{\Delta_i+\Delta_{i+1}}f_{i+1}-f_i+\frac{\Delta_i}{\Delta_i+\Delta_{i+1}}f_{i-1}-\frac{\Delta_i\Delta_{i+1}}{2}\frac{(P_e-P)}{T}\left[1+\left(\frac{f_{i+1}-f_{i-1}}{\Delta_i+\Delta_{i+1}}\right)^2\right]^{3/2}=0 \tag{16}$$

Here 'Δ' denotes the distance of two neighbouring nodes projected to the x-direction:

$$\Delta_i=x_i-x_{i-1} \tag{17}$$

The Newton–Raphson method is used to solve the non-linear equation (16). The iterative procedure will terminate when the residual of (16) satisfies the following convergence criteria:

$$\|R^k(f)\|<\varepsilon_1 \tag{18}$$

Here k is the iteration number.

4. MESH SMOOTHING

The membrane displacement leads to the moving of mesh nodes on the fluid boundary. If the nodes on the compliant wall are alone moved while the interior nodes are kept intact, poor-quality or even over-lapping cells may appear. This could affect the accuracy of the numerical algorithm or stop the calculation from proceeding. The objective of the mesh smoothing is to smooth out the disturbance from these boundary nodes into the whole domain and ensure a good mesh quality throughout the computing procedure. A spring analog model is used to achieve this. In this numerical scheme, each face is replaced by a spring pulling its two nodes towards each other. The mesh smoothing procedure is completed when all the nodes reach a state of equilibrium. This method avoids the topology change thus is much easier to implement than the point inserting and deleting technique. The movement of mesh nodes is determined by

$$\frac{\mathrm{d}\mathbf{r}^{(i)}}{\mathrm{d}\tau}=\sum_{j=1}^{\mathrm{nb}}\mathbf{F}^{(ij)}=\sum_{j=1}^{\mathrm{nb}}k^{(ij)}(\mathbf{r}^{(j)}-\mathbf{r}^{(i)}) \tag{19}$$

where $\mathbf{r}^{(i)}$ and $\mathbf{r}^{(j)}$ are the position vectors of node i and j, $\mathbf{F}^{(ij)}$ is the pulling force exerted on node i by spring 'ij', $k^{(ij)}$ is the stiffness coefficient of spring 'ij'. 'nb' stands for all the

Copyright © 2005 John Wiley & Sons, Ltd.

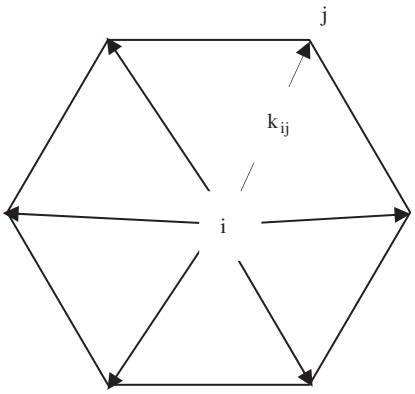

Figure 3. Spring analogy model for the mesh smoothing.

neighbouring nodes which are connected to node i (see Figure 3). τ is the pseudo-time. Since **r** appears on both sides of Equation (19), an iterative approach is used to solve it.

5. COUPLING STRATEGY

The fluid and membrane equations form a coupled system. The fluid pressure on the membrane is determined by solving the Navier–Stokes equation. The difference between the fluid and ambient pressure on the membrane will determine the shape of the membrane through Equation (15), similarly the shape of the membrane will also dictate the flow field. The computational domain for the fluid is modified by updating the membrane shape. A steady solution is obtained only when both the change in the flow field and the displacement in the membrane are negligibly small. An iterative scheme is implemented to capture this steady solution. This scheme can be summarized as

(1) An initial membrane shape is chosen with an initial flow field. A time marching is performed on this geometry until a steady state is reached. The flow field is considered to have reached the steady state if the following condition is satisfied:

$$\| p^n - p^{n-1} \| \leqslant \varepsilon_2 \tag{20}$$

While within each time step, the convergence of the pressure-correction procedure is determined by another condition:

$$\| R_c^m \| < \varepsilon_3 \tag{21}$$

Here R_c is the residual in the continuity equation. m is the iteration number of a *SIMPLE* loop.

(2) Equation (16) is solved using the converged pressure field. After the nodes displacement of the membrane is computed, these nodes are moved according to the displacement.

Copyright © 2005 John Wiley & Sons, Ltd.

(3) The mesh is smoothed using (19) to improve the mesh quality. All the boundary nodes (including those on the membrane) are intact in the smoothing procedure.
(4) A time marching is performed again on the new geometry; the solution on the old geometry is used as a initial condition.
(5) This iteration procedure will terminate only when both the convergence criteria in (20) for the flow field and (22) for the membrane displacement are satisfied:

$$\|f^l - f^{l-1}\| \leqslant \varepsilon_4 \tag{22}$$

l is the iteration number for this 'steady-state capturing' scheme.

In this work, the convergence criteria for the pressure field and membrane displacement are:

$$\varepsilon_1 = 1 \times 10^{-6}, \quad \varepsilon_2 = 3 \times 10^{-4}, \quad \varepsilon_3 = 3 \times 10^{-6}, \quad \varepsilon_4 = 5 \times 10^{-6} \tag{23}$$

It is found that a very tight convergence criterion for the pressure field is not necessary as the membrane shape is updated at frequent intervals, and the pressure is very sensitive to the geometry of the computational domain. However, very loose convergence criteria for the pressure will lead to divergence of the whole system or an inaccurate final solution. The values in (23) are determined by numerical experiments. The flow chart of this algorithm used in the code is shown in Figure 4.

Other measures are also taken to avoid divergence or to make the computation converge faster. Some of these measures are summarized as follows:

(a) When β is large (>30), in order to capture the steady solution, one may start with a smaller β; after the solution has converged to some degree (not necessary to satisfy the condition in (22)), increase the value of β slightly. By doing it 'step-by-step', it is much easier to obtain a solution then directly jumping to a large β.
(b) A relaxation in the membrane displacement in needed when β is even large (>90). Instead of using (16), the following amendment is used to calculate the membrane displacement:

$$\tilde{f}^l = \alpha f^l + (1 - \alpha) f^{l-1} \tag{24}$$

where $\tilde{f}^l$ is the displacement used to move the nodes and f^l is the displacement calculated using (16). α is a relaxation factor ranging from 0.1 to 0.9.
(c) One may need to pay some attentions to the convergence criteria ε_3 of the continuity equation in the *SIMPLE* loop. A very loose one may cause an inaccurate solution while a too tight one is a waste of computer time. It is found that a value from 1×10^{-6} to 1×10^{-5} is appropriate for the simulations in this study. It is also found that the convergence behaviour of the *SIMPLE* algorithm is strongly associated with the mesh quality. Convergence is much faster on a nearly orthogonal mesh than on a highly skewed one.

Copyright © 2005 John Wiley & Sons, Ltd.

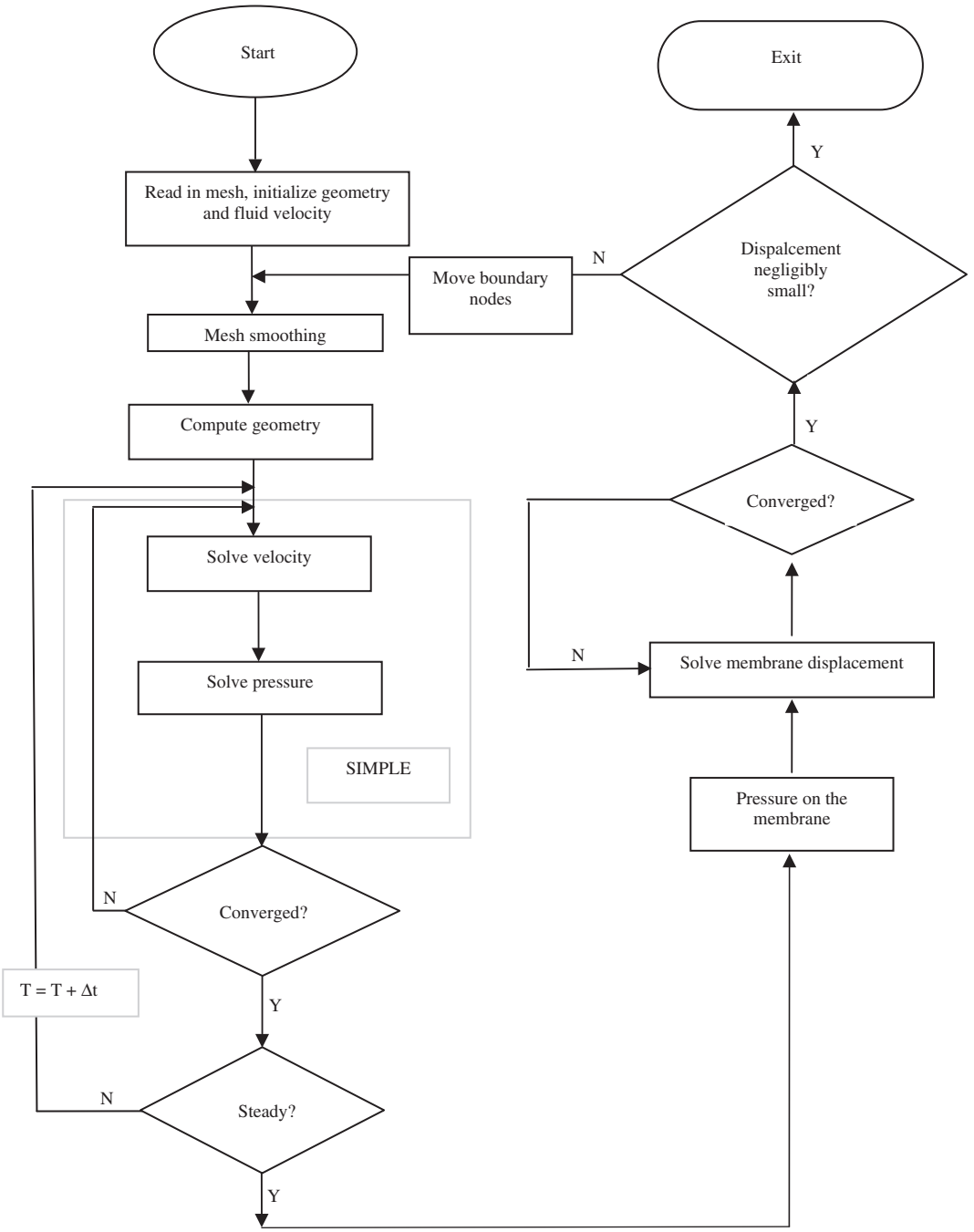

Figure 4. Flow chart of the algorithm used in the code.

Copyright © 2005 John Wiley & Sons, Ltd.

6. NUMERICAL SIMULATIONS AND DISCUSSIONS

6.1. Computer code and validations

The simulations in this paper are performed using *UNCFV3D*, an in-house research code developed in Institute of High Performance Computing (IHPC). This code is a 2D/3D finite volume solver which uses the *SIMPLE* algorithm to solve incompressible Navier–Stokes equation on an unstructured mesh. The basic numerical method is based on that described in References [27, 28]. The code is still under development. At this moment, some validations have been completed for 2D and 3D laminar flows.

(a) *Two dimensional Poiseuille flow*: Before solving the fluid–membrane problem, a two-dimensional channel flow with rigid walls is tested. The computational mesh is shown in Figure 5. The stream-wise velocity profiles at place $x = 10$ for both the analytical and numerical solutions are shown in Figure 6. Two numerical results are obtained, one using the mesh in Figure 5 and the other using a more refined mesh (about twice the mesh number). From Figure 6 one can see that both numerical solutions match very well with the analytical one. In the analytical solution, it can be seen that the maximum velocity on the centre-line is 1.5 of the bulk velocity. Comparing this maximum velocity with numerical results, it is seen that the error is 1.2% for the normal mesh and 0.7% for the more refined mesh. As a compromise of CPU time and accuracy, the mesh in Figure 5 is used in all the subsequent simulations.

6.2. Control parameters in the fluid–membrane system

The parameters used in the simulation are the same as those in Reference [16]. They are listed in Table I.

6.3. Numerical results

Three parameters Re, T and P_e are chosen as the control parameters. How the membrane behaves with the variation of these parameters will be presented in the section. In order to compare with the result in Reference [16], two new parameters β and γ are introduced and

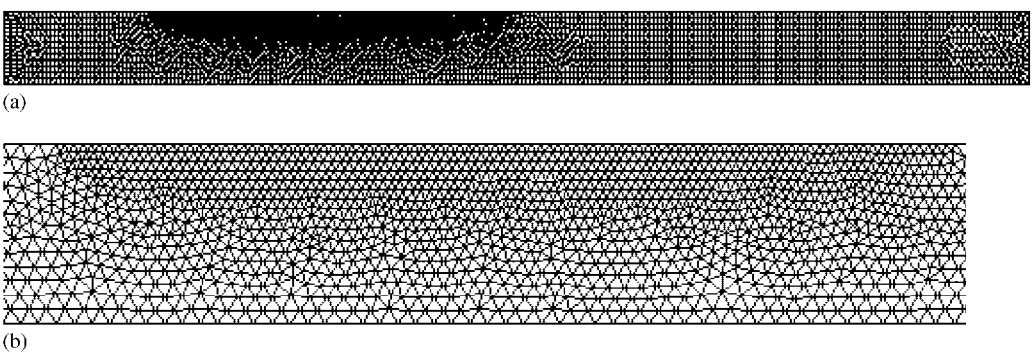

Figure 5. The mesh of the fluid domain with 2587 triangles and 4822 nodes: (a) mesh in the original scale; and (b) zoom in near the compliant wall.

Copyright © 2005 John Wiley & Sons, Ltd.

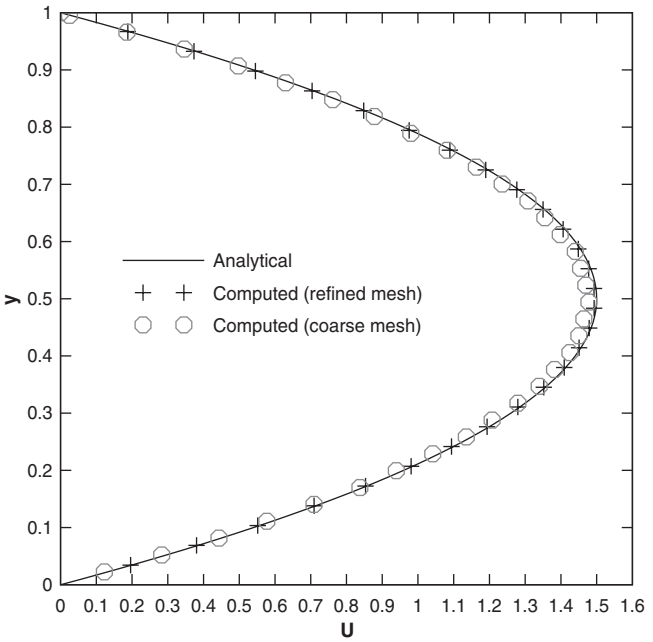

Figure 6. Velocity profile at $x = 10$ of a rigid channel solution. Solid line is the Poiseuille solution; circle is the numerical solution using the mesh in Figure 5 and cross is the numerical solution using a more refined mesh.

Table I. Values of parameters used in the simulation.

$\mu^* = 1 \times 10^{-3}$ Pa s	$\rho^* = 10^3$ kg m^{-3}	$D = 10^{-2}$ m
$L_1^* = 2 \times 10^{-2}$ m	$L_c^* = 5 \times 10^{-2}$ m	$L_2^* = 7 \times 10^{-2}$ m
$P_{e0}^* = 0.93$ Pa	$T_0^* = 1.61$ N m^{-1}	$U_0 = 1 - 4 \times 10^{-2}$ m s^{-1}

the tension and the pressure are converted to their non-dimensional form using Equation (25):

$$T = 1 \times 10^7 (T_0^*/\beta Re^2), \quad P_e = 1 \times 10^5 (P_{e0}^*/\gamma Re^2) \tag{25}$$

where T_0^* and P_{e0}^* are the values listed in Table I. Now the control parameters are Re, β and γ. This formulation is also given in Reference [31]. For the derivation of (25), please refer to the appendix.

6.3.1. Different membrane shapes with the variation of tension scaling factor β. The first numerical result shows different membrane shapes with the variation of β. The pressure scaling factor γ is set to unity and Re is set to 300. Figure 7(a)–(g) shows the mesh of a steady solution for β ranging from 1 to 180. When β is small (T is large), the membrane deformation is very small and a solution similar to that of a rigid channel flow is obtained. With the increase of β, the membrane is pushed further downwards and deformation increases. The point

Copyright © 2005 John Wiley & Sons, Ltd.

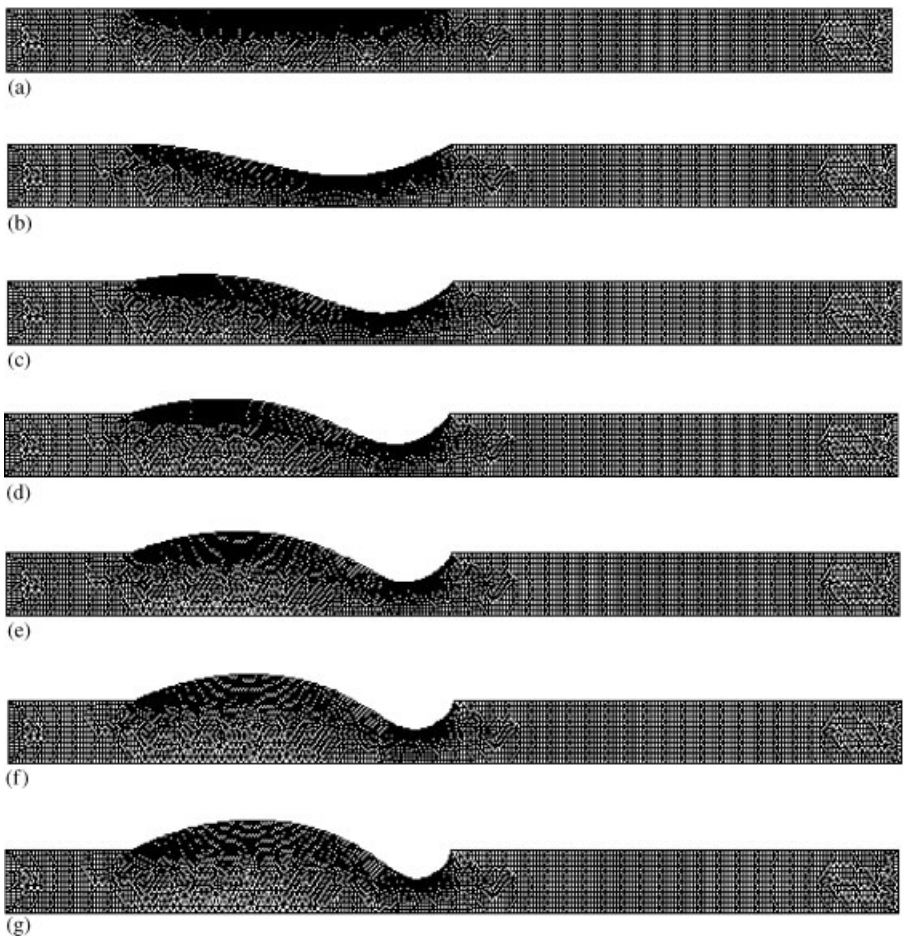

Figure 7. Meshes of a steady solution for different tension scaling factors at $Re = 300$ and $\gamma = 1.0$: (a) $\beta = 1$; (b) $\beta = 30$; (c) $\beta = 60$; (d) $\beta = 90$; (e) $\beta = 120$; (f) $\beta = 150$; and (g) $\beta = 180$.

of greatest constriction will move slightly downstream from the mid-point of the membrane with the increase of β. At certain level of β (about 30), an inflection point will appear at the upstream half of the membrane. If β increases further, the membrane will bulge out at the upstream half while the point of greatest constriction will continue to move downstream. However, the minimum height of the channel will increase slightly with the increase of β. The results match well with the prediction of Lou and Pedley [16]. In Figure 8, the membrane shapes from the present simulation are compared with that in Reference [16] for selected β. From this figure one can see that the deformation predicted in this paper is slightly less than that of Lou and Pedley [16] and the largest difference appears near the point of greatest constriction. The y-co-ordinate of this point is plotted against β in Figure 9. Luo and Pedley's [16] prediction is also plotted in this figure for comparison. For all cases computed, the largest difference in deformation is about 5%. Further investigation on the solution using a more

Copyright © 2005 John Wiley & Sons, Ltd.

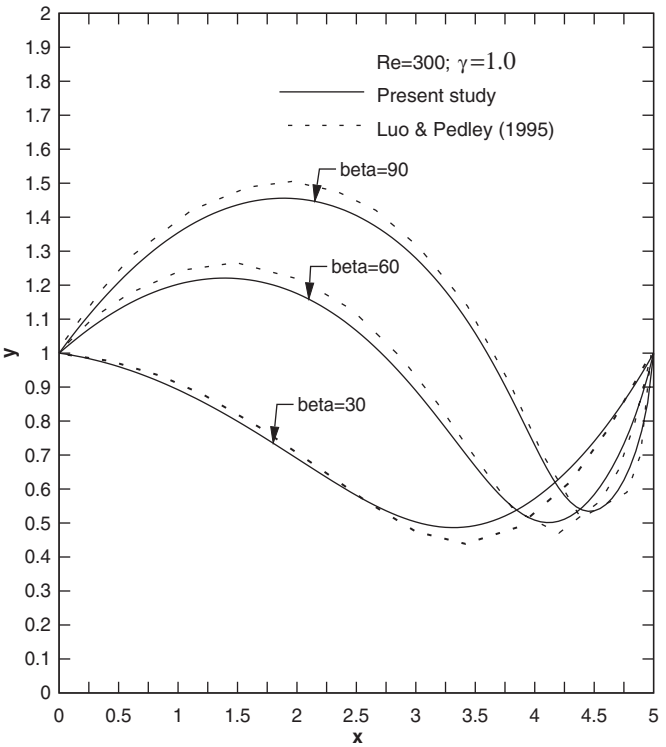

Figure 8. The membrane shapes at for different tension scaling factor $\beta = 30$, 60, 90. Solid line is result of the present simulation and dash line is the result from Reference [16].

refined mesh (about twice the mesh number) shows that a mesh-independent solution has been obtained. Thus the 5% difference is possibly not associated with mesh resolution. The reason for this difference needs further investigation.

6.3.2. Different membrane shapes with the variation of Re numbers. The *Re* number effect on the membrane shape is studied in this section. Figure 10 shows the membrane shape at *Re* number ranging from 1 to 400. The tension scaling factor β is 30 and pressure scaling factor γ is 1.0. For small *Re* numbers (1–100), the maximum displacement is located near the mid-point of the membrane. The displacement of the membrane is almost symmetric. The maximum displacement decreases slightly with the increase of *Re* number. With a further increase of *Re* number to 200, the maximum displacement will increase and the moving of the point of greatest constriction towards the downstream direction is observed. The membrane shape greatly deviates from a symmetric one. If *Re* number increases from 200 to 400, maximum displacement will decrease again and the point of greatest constriction will move further downstream. Furthermore, an inflection point will appear at the upstream part of the membrane and this part of the membrane will become more open as *Re* number increases. A bulging region in the upstream part of the membrane is also observed at *Re* number 400.

Copyright © 2005 John Wiley & Sons, Ltd.

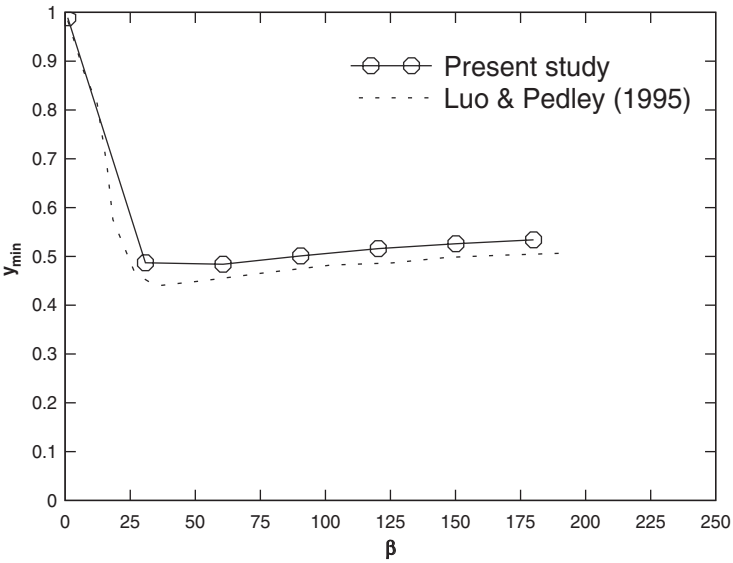

Figure 9. The y co-ordinate of the point of greatest constriction as a function of β.

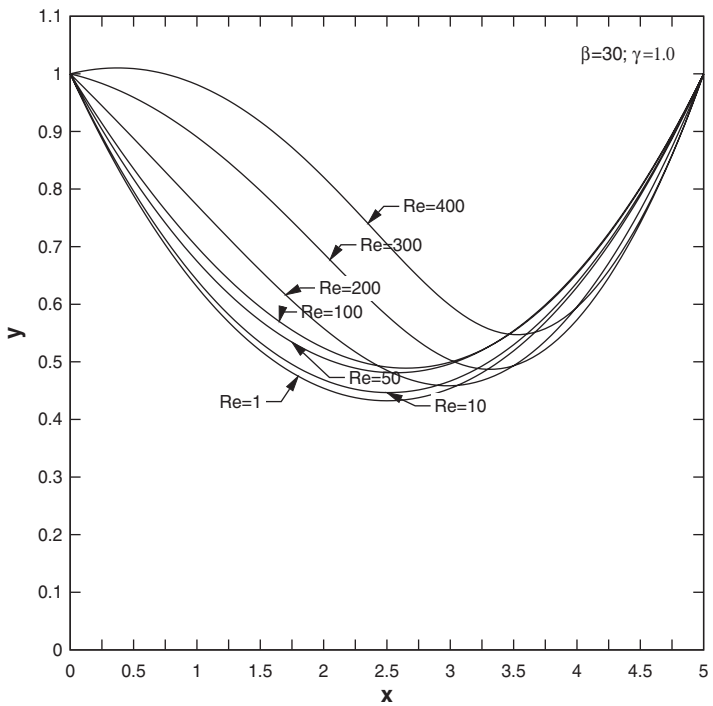

Figure 10. Membrane shapes at different Re numbers for a fixed β and γ.

Copyright © 2005 John Wiley & Sons, Ltd.

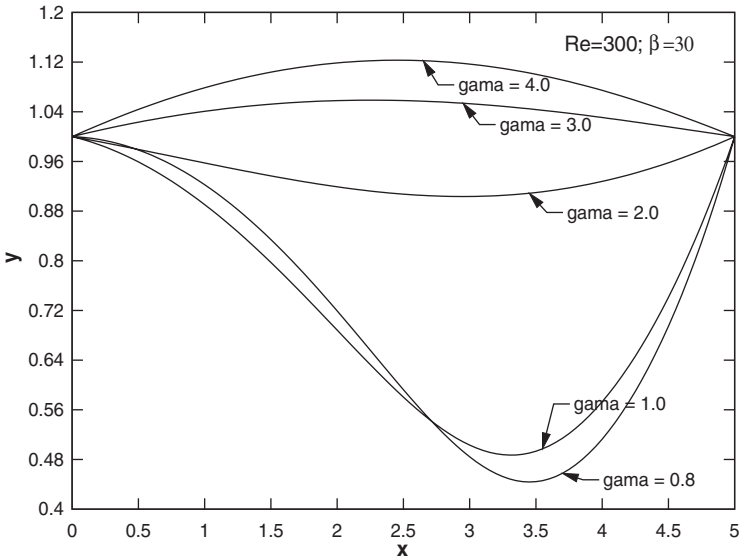

Figure 11. Membrane shapes at different γ for a fixed Re and β.

6.3.3. The different membrane shapes with the variation of γ. The effect of ambient pressure on the shapes of the membrane is also studied. Figure 11 shows the membrane shape at γ ranging from 0.8 to 4.0. The Re number for these simulations is 300 and the tension scaling factor β is 30. It is observed in this figure that a small γ has the similar effect as a large β. With very large γ (3.0 or 4.0), or very smaller ambient pressure, the whole membrane will bulge out. This result is reasonable and agrees with that of commonsense.

6.3.4. Pressure drop with the variation of Re and β. Pressure drop is closely related to the fluid carrying capability in physiological flows, and therefore is a very important parameter which needs some investigation. Figure 12 shows the overall pressure drop ($\Delta P^* = P_1^* - P_0^*$) along the channel as a function of Re number at three different β (10, 20 and 30). It is observed that for almost all cases computed, the pressure drop for a compliant wall is higher than that for a rigid wall at the same Re number and γ (the case of $Re = 100$ and $\beta = 20$ is the only exception). For $\beta = 10$, the pressure drop is linearly dependent on Re number, similar to that of Poiseuille solution for a rigid channel but with slightly larger slope. For $\beta = 20$, the trend is almost the same as that of $\beta = 10$, but in the Re number ranging from 50 to 100, a 'flat' region appears, this indicates that pressure drop remains the same as Re number increase. For the $\beta = 30$ case, the trend is the same as $\beta = 10$ but the slope is much higher.

6.3.5. Separation bubbles. According to the discussions in Section 6.3.1, for small β, no separation is possible as a result of very small membrane displacement. At certain level of β, flow separation is inevitable because of large displacement. For the case of $Re = 300$ and $\gamma = 1.0$, separation first appears at $\beta \approx 20$. This separation bubble is located at the downstream

Copyright © 2005 John Wiley & Sons, Ltd.

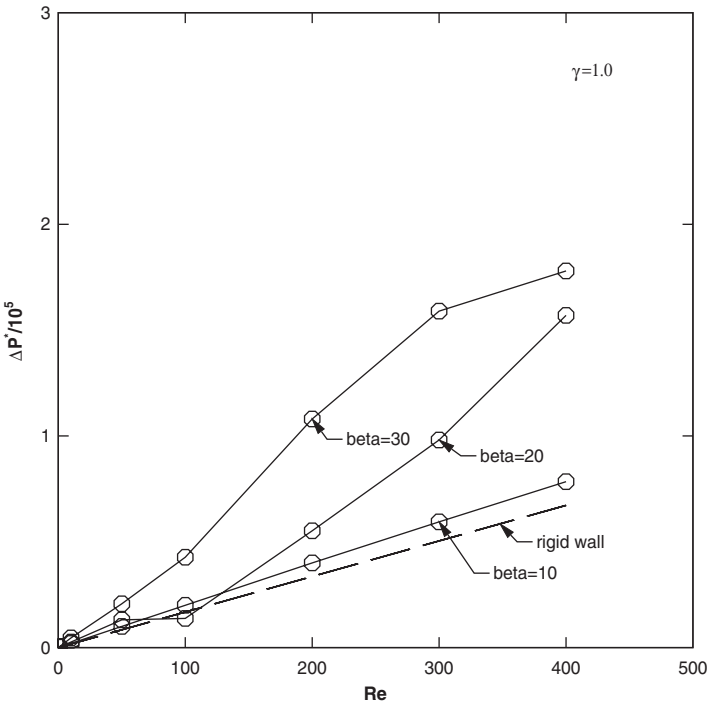

Figure 12. Pressure drop against *Re* number and tension scaling factor β.

end of the membrane, partially on the membrane and partially on the rigid wall. For the three cases of very large β (120, 150 and 180), besides the downstream bubble, another slightly smaller bubble also exists on the upstream part of the membrane. Two cases ($\beta = 30$ and 180) with flow separations are shown in Figure 13(a) and (b), both the velocity magnitude contours and streamlines are plotted. Figure 14 shows the location (x co-ordinate) of the separation and reattachment point at different level of β at fixed *Re* number and γ. From Figure 14, one can see that the size of the downstream bubbles are almost the same for the six cases and the bubble centre moves slightly towards the downstream direction as β increases. As to the small upstream bubbles, the size increases as β increases and the bubble centre also moves towards the downstream direction. These observations to the flow pattern may have a significant effect on the transport of the fluid (e.g. blood) and thus might be of great interest to physicians.

7. CONCLUSION AND FUTURE WORK

In this paper, we have conducted a preliminary investigation on a 2D channel flow with a partially compliant wall through numerical simulations. All the computations are done using an in-house CFD code developed at IHPC. The finite volume–finite difference approach is implemented to solve a fluid–membrane coupled system. The formulation of this approach is

Copyright © 2005 John Wiley & Sons, Ltd.

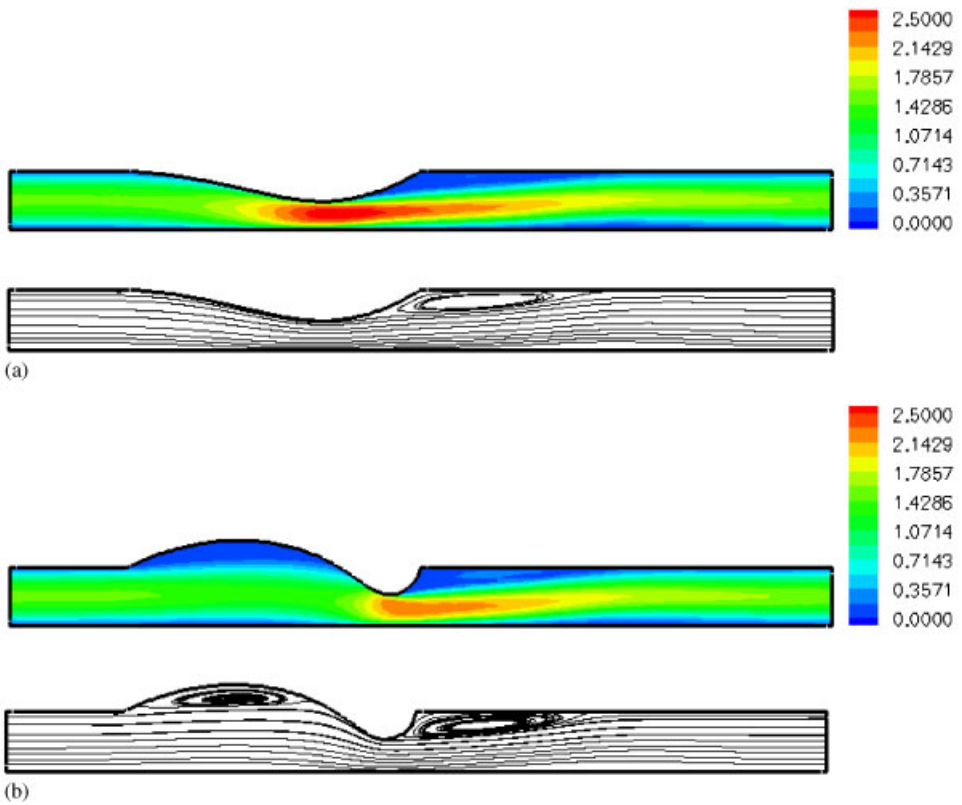

Figure 13. Velocity magnitude contours and streamlines at $Re = 300$ and $\gamma = 1.0$: (a) $\beta = 30$; and (b) $\beta = 180$.

simpler than that of a fully coupled FEM. Compared with those in the literature, satisfactory results are obtained using the present approach. Further studies regarding the numerical accuracy are presently underway, especially the study of the influence of several converging (stopping) criteria (see Sections 3 and 5) on the overall accuracy.

As an extension of the present work, unsteady analysis will be conducted. The unsteadiness will require a more complicated fluid–structure interaction (FSI) model involving the inertia effect of the membrane and the exchange of boundary information between the fluid and the membrane. Furthermore, an ALE re-formulation of the Navier–Stokes equation is also required due to the mesh movement. However, in the FVM, such re-formulation is straightforward by adding a mesh moving velocity and is just a minor change in the governing equation of the fluid. This feature is another advantage of this numerical method over FEM. There are also some other avenues for further research. They may include the longitudinal variation effect of the membrane tension and some more complicated models for the membrane, such as the beam model.

Copyright © 2005 John Wiley & Sons, Ltd.

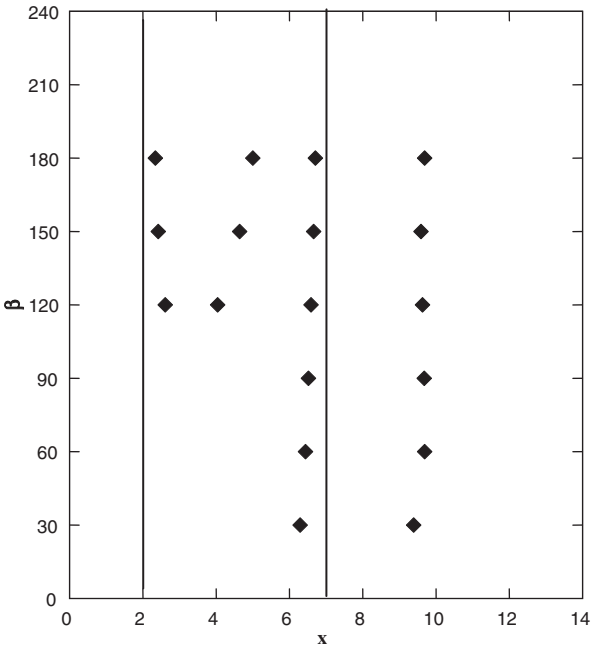

Figure 14. x-co-ordinate of the separation and re-attachment points at five different level of β for $Re = 300$ and $\gamma = 1.0$. Two vertical lines indicate the span of the membrane.

APPENDIX A: DIMENSIONLESS FORMULATION

The non-dimensional governing equations for the fluid in a differential form are written as

$$\frac{\partial \mathbf{v}}{\partial t} + (\mathbf{v} \cdot \nabla)\mathbf{v} - \frac{1}{Re}\nabla^2 \mathbf{v} = -\nabla P$$
$$\nabla \cdot \mathbf{v} = 0 \tag{A1}$$

The definitions of the non-dimensional variables are as following:

$$x = x^*/D, \quad y = y^*/D, \quad \mathbf{v} = \mathbf{v}^*/U_0, \quad t = t^* U_0/D, \quad P = P^*/(\rho^* U_0^2), \quad Re = \rho^* U_0 D/\mu^* \tag{A2}$$

The ones with * are the original (dimensional) variables. D is diameter of the channel and is chosen as the characteristic length. U_0 is the bulk velocity at the inlet and is chosen as the characteristic velocity.

Similarly, the non-dimensional governing equation for the membrane displacement is

$$-\frac{Tf''}{(1+f'^2)^{3/2}} + (P - P_e) = 0 \tag{A3}$$

The definitions of the non-dimensional variables are:

$$f = f^*/D, \quad T = T^*/(\rho^* U_0^2 D), \quad P_e = P_e^*/(\rho^* U_0^2) \tag{A4}$$

Copyright © 2005 John Wiley & Sons, Ltd.

By a re-formulation of the non-dimensional pressure and tension and substituting the quantities in Table I, the equations in (25) can be derived very easily.

$$P_e = P_e^*/(\rho^* U_0^2) = (P_e^*/Re^2)(\rho^* D^2/\mu^{*2}) = 10^5 (P_e^*/Re^2)$$
$$T = T^*/(\rho^* U_0^2 D) = (T^*/Re^2)(\rho^* D/\mu^{*2}) = 10^7 (T^*/Re^2) \tag{A5}$$

ACKNOWLEDGEMENTS

This work is supported by Institute of High Performance Computing (IHPC) through an internal research project IHPC/02-100325-EOM.

REFERENCES

1. Conrad WA. Pressure-flow relations in collapsible tubes. *IEEE Transactions in Biomedical Engineering* 1969; **BME-16**:248–295.
2. Brower RW, Scholten C. Experimental evidence on the mechanism for the instability of flow in collapsible vessels. *Journal of Biomechanical Engineering* (ASME) 1975; **13**:389–845.
3. Bertram CD. Two modes of instability in a thick-walled collapsible tube conveying a flow. *Journal of Biomechanics* 1982; **15**:223–224.
4. Bertram CD. Unstable equilibrium behaviour in collapsible tubes. *Journal of Biomechanics* 1986; **19**:61–69.
5. Bertram CD, Raymond CJ, Pedley TJ. Mapping of instabilities for flow through collapsed tubes of different length. *Journal of Fluids and Structures* 1990; **4**:125–154.
6. Bertram CD, Raymond CJ, Pedley TJ. Application of nonlinear dynamics concepts to the analysis of self-excited oscillations of a collapsible tube conveying a fluid. *Journal of Fluids and Structures* 1991; **5**:391–426.
7. Bertram CD, Godbole SA. LDA measurements of velocities in a simulated collapsed tube. *Journal of Biomechanical Engineering* (ASME) 1997; **119**:357–363.
8. Bertram CD, Castles RJ. Flow limitation in uniform thick-walled collapsible tubes. *Journal of Fluids and Structures* 1999; **13**:399–418.
9. Gavriely N, Shee TR, Cugell DW, Grotberg JB. Flutter in flow-limited collapsible tubes: a mechanism for generation of wheezes. *Journal of Applied Physiology* 1989; **66**:2251–2261.
10. Huang L, Quinn SJ, Ellis PDM, Ffowcs Williams JE. Biomechanics of snoring. *Endeavour* 1995; **19**:96–100.
11. Shapiro AH. Steady flow in collapsible tubes. *Journal of Biomechanical Engineering* (ASME) 1977; **99**: 126–147.
12. Cancelli C, Pedley TJ. A separated-flow model for collapsible-tube oscillations. *Journal of Fluid Mechanics* 1985; **157**:375–404.
13. Jensen OE, Pedley TJ. The existence of steady flow in a collapsed tube. *Journal of Fluid Mechanics* 1989; **206**:239–374.
14. Matsuzaki Y, Matsumoto T. Flow in a two-dimensional collapsible channel with rigid inlet and outlet. *Journal of Biomechanical Engineering* (ASME) 1989; **111**:180–184.
15. Pedley TJ. Longitudinal tension variation in collapsible channels: a new mechanism for breakdown of steady flow. *Journal of Biomechanical Engineering* (ASME) 1992; **114**:60–67.
16. Luo XY, Pedley TJ. A numerical simulation of steady flow in a 2-D collapsible channel. *Journal of Fluids and Structures* 1995; **9**:149–174.
17. Luo XY, Pedley TJ. A numerical simulation of unsteady flow in a 2-D collapsible channel. *Journal of Fluid Mechanics* 1996; **314**:191–225.
18. Heil M. Stokes flow in collapsible tubes: computation and experiment. *Journal of Fluid Mechanics* 1997; **353**:285–312.
19. Heil M. Stoke flow in an elastic tube—a large-displacement fluid–structure interaction problem. *International Journal for Numerical Methods in Fluids* 1998; **28**:243–265.
20. Cai ZX, Luo XY. A fluid-beam model for flow in a collapsible channel. *Journal of Fluids and Structures* 2003; **17**:125–146.
21. Bathe KJ, Kamm RD. A fluid–structure interaction finite element analysis of pulsatile blood flow through a complaint stenotic artery. *Journal of Biomechanical Engineering* (ASME) 1999; **121**: 361–369.
22. Shim EB, Kamm RD. Numerical simulation of steady flow in a compliant tube or channel with tapered wall thickness. *Journal of Fluids and Structures* 2002; **16**(8):1009–1027.

Copyright © 2005 John Wiley & Sons, Ltd.

23. Takemitsu N, Matunobu Y. Numerical calculation of two-dimensional flow in the channel with a partially compliant wall. *Fluid Dynamics Research* 1988; **4**:1–14.
24. Demirdzic I, Martinovic D. Finite volume method for thermo-elasto-plastic analysis. *Computer Methods in Applied Mechanics and Engineering* 1993; **109**:331–349.
25. Demirdzic I, Muzaferija S. Finite volume method for stress analysis in complex domains. *International Journal for Numerical Methods in Engineering* 1994; **37**:3752–3766.
26. Slone KA, Pericleous K, Bailey C, Cross M. Dynamic fluid structure interaction using finite volume unstructured mesh procedures. *Computers and Structures* 2002; **80**:371–390.
27. Demirdzic I, Muzaferija S. Numerical method for coupled fluid flow, heat transfer and stress analysis using unstructured moving meshes with cells of arbitrary topology. *Computer Methods in Applied Mechanics and Engineering* 1995; **125**:235–255.
28. Demirdzic I, Muzaferija S, Peric M. Advances in computation of heat transfer, fluid flow, and solid body deformation using finite volume approaches. *Advances in Numerical Heat Transfer*, vol. 1, Chapter 2, 1997.
29. Ferziger JH, Peric M. *Computational Methods for Fluid Dynamics*, Chapter 8. Springer: Berlin, 1996.
30. Luo XY, Pedley TJ. The effects of wall inertia on flows in a two-dimensional collapsible channel. *Journal of Fluid Mechanics* 1998; **363**:253–280.
31. Pedley TJ, Luo XY. Modeling flow and oscillations in collapsible tubes. *Theoretical and Computational Fluid Dynamics* 1998; **10**:277–294.

Copyright © 2005 John Wiley & Sons, Ltd.